Contact Angle Influence in Capillary Flows

D. Ferreira, D. Fiorini, J. André, and M. Mendez
Instituto Superior Técnico, Universidade de Lisboa, Portugal

December 2022

Abstract

This work addresses the impact of surface tension forces on the dynamics of an inertia-driven capillary rise of a gas-liquid interface. Several experimental campaigns were conducted, cross-checking the impact of surface tension forces on different geometries. The experimental campaigns used three different facilities. The first facility carried out sessile droplet tests to obtain the angle of contact between a liquid interface and a solid surface. In static conditions, the "static contact angle" is a property of the fluid/solid combination, which in this work concerned HFE7200 (hydrofluoroether) and quartz surfaces. The second facility is a quasi-capillary U-tube set-up where tests on the interface deformation following a pressure step were performed in a separate experimental campaign. The results from the latter were compared with the ones obtained by the third facility studied in this work, hence requiring the characterization of the optical distortion in cylindrical tubes and the development of a corrective routine. The third facility concerns two parallel plates in close vicinity where a gas-liquid interface is forced to rise by means of a pressure step. The facility allowed to test integral models developed for capillary tubes to explore the possibility of measuring the impact of surface tension and the role of the contact angle on the inertia-driven capillary rise between the parallel plates.
Keywords: Capillary Flow, Contact Angle, Optical Distortion

1. Introduction

The contact angle is a boundary condition for the shape of any liquid-gas interface in contact with a solid surface. It represents an important parameter to model the capillary pressure drop at the interface and plays an important role in the motion of the interface in capillary-dominated applications such as coatings, powder processing, and fuel injector manufacturing [2] [31] [22].

In static conditions, as is the case of a sessile droplet, the *equilibrium* contact angle, θ_{Young}, is given by Young's relation $\gamma_{SV} - \gamma_{SL} = \gamma cos(\theta_{Young})$, where γ_{SV} and γ_{SL} are the solid-vapor and solid-liquid interface energies respectively and γ is the surface tension. θ_{Young} varies largely depending on the characteristics of the substrate and the atmosphere surrounding the droplet. Consequently experiments on sessile droplets characterize only the *static* contact angle θ_S.

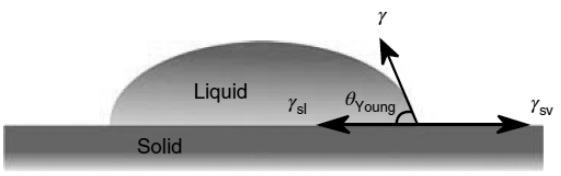

Figure 1: Visualisation of the *static* contact angle of a generic droplet [14]

When the line of contact with the solid surface moves, the angle is called *dynamic* (θ_D), and it becomes a function of the velocity and the acceleration of the contact line. [14]

Traditional models for the surface tension forces at the interface and the dynamic contact angle have characterised mainly small test-case applications dominated by capillary and viscous forces [17] [26] [25]. However, emerging technologies for space applications require a deeper understanding of free interface flows driven by the balance of capillary and inertial forces. These types of flow play an essential role in orbital manoeuvres where the liquids stored within the spacecraft tanks are not bounded by gravity. In these circumstances, the liquid sloshing motion occurs at low Bond numbers, and the resulting flow is capillary dominated, i.e. the dominant forces are surface tension mechanisms, which condition the interface's response to the accelerations imposed on the tank. For example, [20] considered the performance of Ariane 5's A5ME upper stage, where the controller struggled to cope with the time dependant inertia tensor due to the sloshing motion under a slew manoeuvre, which led to a high number of thrust activations. The authors observed that better control and understanding of this phenomena would lead to quicker manoeuvres, settling times and higher fuel efficiency in these spacecraft.

At the von Karman Institute, the impact of surface tension and the response of liquid interfaces to step acceleration impulses is currently studied in the framework of *Project Slosh II*, where the main focus is on the sloshing of cryogenic liquids and *Project Minerva* where the impact of inertial forces on the modelling of the fluid/surface interaction is assessed for coating applications.

In this project, we studied the impact of surface tension forces in a 2D facility where the motion of a liquid interface is pressure driven between a narrow channel. The target fluid is HFE7200, a synthetic fluid mimicking the properties of cryogenic propellant (e.g. liquid oxygen). We extend the formulation of capillary-driven flows for the case of a forced pressure rise and evaluate the impact of contact angle term on the interface rise. The *dynamic* contact angle is assessed using direct interface extrapolation techniques and indirect methods based on the model for the interface rise. This data is compared with interface observations with sessile droplets and the case of an axially-symmetric meniscus in cylindrical channels (U-tube facility). The dynamic contact angle experimental results are compared both with traditional dynamic contact angle correlations and new correlations developed over the course of *Project Slosh II* and more specifically, Domenico Fiorini's Phd work conducted at the von Karman Institute in collaboration with KU Leuven University [10].

2. Modeling of the interface shape and its motion

2.1. Interface shape model

2.1.1 Sessile droplet

We conducted a sessile droplet test campaign to determine the static contact angle for HFE7200. This technique consists in recording a video of a drop of liquid on a quartz plate and then selecting the contact angle by fitting the droplet surface with a physical model of the interface that depends on the contact angle. The physical model considered was based on a static force balance [6]. The forces considered are the hydro-static pressure difference across the droplet surface and surface tension and the balance reads:

$$\rho g z = \sigma \vec{\nabla}.\vec{n} \tag{1}$$

In 1, ρ is the density of the fluid, g is the gravitational acceleration, σ is the surface tension and $\vec{n}$ represents a normal unitary vector to its surface. Thus, considering the coordinate system for the droplet represented in figure 2 and its axially-symmetric properties, the curvature term in equation 1 can be obtained and that results in equation 2.

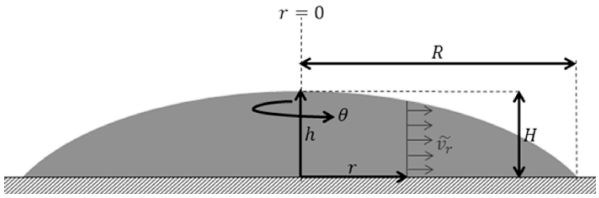

Figure 2: Coordinate system droplet [9]: h - coordinate for the distance between the liquid/gas interface and the solid surface; r - radial coordinate; θ - axial coordinate; R - radius of the droplet; H - height of the droplet

$$h_{rr} = \frac{h}{l_c^2}(1 + h_r^2)^{3/2} - \frac{h_r}{r} \tag{2}$$

In equation 2, $l_c = \sqrt{\frac{\sigma}{\rho g}}$ is defined as the *capillary length* typical of the fluid and the subscripts denote the order of the derivative of the interface height with respect to r. This equation can be solved by imposing Neumann type boundary conditions as expressed in equation 3. Hence, we calculated the *static* contact angle by fitting the experimental points of the surface with equation 2, using the contact angle as a free parameter of the regression, which is elaborated further on in section 4. [3]

$$\begin{cases} h_r = 0, & r = 0 \\ h_r = -tan(\theta_{static}), & r = R \end{cases} \tag{3}$$

2.1.2 Symmetric meniscus

The same procedure is applied to the meniscus in the quasi-capillary U-tube, which has the coordinate system described in figure 3.

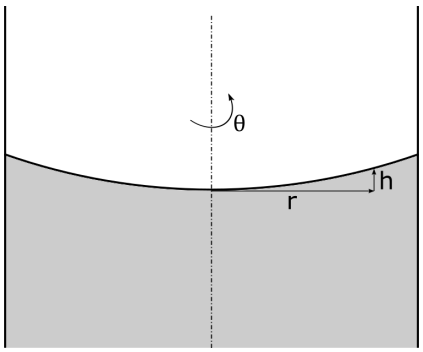

Figure 3: Coordinate system for the quasi-capillary U-tube interface (cylindrical coordinates): h is the coordinate for the height of a generic point with respect to the lowest point in the meniscus; r is the radial coordinate; θ is the axial coordinate

In this case the boundary conditions are in 4, where the h_r represents the spatial derivative with respect to r and r_i represents the inner tube radius.

$$\begin{cases} h_r = 0, & r = 0 \\ h_r = 1/tan(\theta_{static}), & r = r_i \end{cases} \tag{4}$$

The quasi-capillary parallel plates use a Cartesian coordinate system to describe the bi-dimensional approximation of the interface, which results in a different equation to describe its interface and boundary conditions to match it, as seen in equations 5 and 6, where w corresponds to the width of the channel.

$$h_{xx} = \frac{h}{l_c^2}(1 + h_x^2)^{3/2} \tag{5}$$

$$\begin{cases} h_x = 0, & x = 0 \\ h_x = 1/tan(\theta_{static}), & x = w/2 \end{cases} \tag{6}$$

The coordinate system used to derive this equation is described in figure 4.

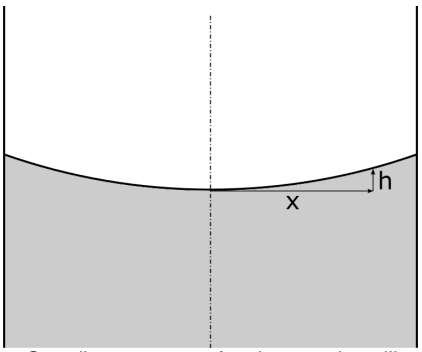

Figure 4: Coordinate system for the quasi-capillary parallel plates interface (bi-dimensional interface - fully developed flow along the length of the length of the channel): h is the coordinate for the height of a generic point with respect to the lowest point in the meniscus; x is the distance to the centre of the channel

2.2. Forced rise model

The *dynamic* contact angle characterization takes place in a facility constituted by a narrow channel closed at the lateral ends and inserted in a closed bath. We induced the liquid rise in the channel by controlling the pressure of the gas phase in the bath via an electronic valve. The rise of the liquid interface is modelled with an integral model based on the force balance on the control volume limited by the dashed lines in figure 5 and on prevailing capillary flow models. [17]

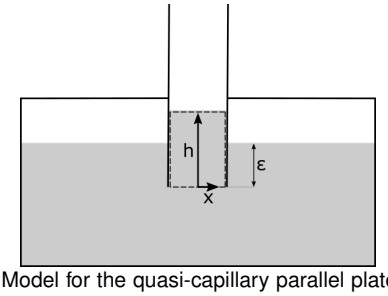

Figure 5: Model for the quasi-capillary parallel plates: x is the coordinate for the width of the channel; h is the coordinate that accounts for the distance from the bottom of the channel; ϵ accounts for the difference between the surface of the liquid and the entrance to the channel

We based the integral model for the rise of the interface on the Lucas-Rideal-Washburn equation [7] [29] described by 7:

$$\frac{dl}{dt} = \frac{1}{8\mu l}[\Delta P' - \rho g l] r_o^2 \tag{7}$$

In equation 7, l refers to the length of the liquid column within the capillary tube; μ is the fluid viscosity; $\Delta P'$ is the capillary pressure, and r_o is the tube radius. This equation has a singularity at the initial stage of the liquid rise in the channel, where it results in an infinite velocity and acceleration, i.e. for $l \to 0$, $\frac{dl}{dt} \to \infty$. This is the effect of the quasi-steady state approximation used to derive it.

Equation 7 has been improved by many authors to include a better description of the phenomena. [17] [26] The added mass term $(h + (\text{added mass}))\ddot{h}$ accounts for the deviation from the hydro-static pressure on the tube entrance with an effective increase in the liquid column inertia and prevents the rise of the singularity at the tube entrance. A second important addition concerns the pressure loss due to the sudden contraction, which is modelled in equation 8 for the case of capillary tubes. This equation is known as the Hagenbach and Couette correction. [4] As an initial approximation, the Hagenbach and Couette coefficient values used are given in Levine's equation, respectively $K_H = \frac{7}{3}$ and $K_C = 4$. These values also correspond to the correlations developed in later works such as [8]. We discuss this assumption for the case of the 2D channel in section 5.

$$\frac{\Delta p_{contraction}}{\rho v^2/2} = K_H + \frac{K_C}{\text{Re}} \tag{8}$$

The complete model for the interface motion in the 2D paralllel plates channel reads as:

$$\begin{aligned} (h + \frac{73}{60}\frac{\delta}{2})\ddot{h} = \frac{\Delta p + \rho g \epsilon}{\rho} + \\ \frac{2\sigma \cos(\theta)}{\rho\delta} - gh - \frac{12\mu}{\rho\delta^2} h\dot{h} \\ -\frac{1}{2}(K_H \dot{h} \mid \dot{h} \mid + \frac{\mu K_C}{\delta\rho}\dot{h}) \end{aligned} \tag{9}$$

The added mass term and the Hagenbach and Couette correction coefficients are compared against the experimental data in section 5.

3. Analysis of axial-symmetric meniscus and correction for optical distortions in cylindrical tubes

One of the objectives of this experimental campaign was to compare the results obtained in the quasi-capillary parallel plates facility with the results obtained from the facility consisting of a cylindrical transparent tube U-shaped, referred to as

a quasi-capillary U-tube since the tube radius is close to the capillary length of HFE7200 $r_i \approx 4l_c$.

During the U-tube experiments, we observed the meniscus movement inside the quasi-capillary U-tube by a camera perpendicular to the quasi-capillary U-tube. The interface was illuminated by a uniform, diffused light source on the opposite side of the camera. This technique results in the blacked-out area on the image, which corresponds to the meniscus' shadow. The shadow of the meniscus is cast onto the tube wall and distorted by its curvature and the different refractive indexes of HFE, quartz and air.

The interface shape is reconstructed by detecting the edge of the shadow. First, however, it is imperative to correct the optical distortion to retrieve the actual shape of the meniscus. The optical distortion can be computed by means of ray-tracing techniques as illustrated in [5] and in [18].

The path of a generic light ray going through a transverse section of the quasi-capillary U-tube is traced from the light source, represented on the left side of figure 6, to the camera, which is on the right side.

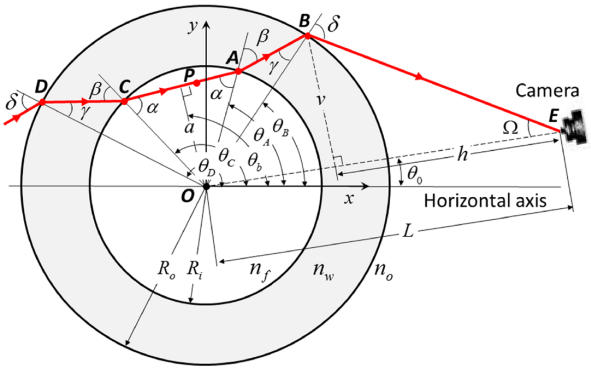

Figure 6: Generic light ray passing through a transversal section of cylindrical tube, where the corresponding refraction and camera angles are represented, figure from [5]

If we consider the camera sensor as a single point, it is possible to associate each light ray with its angle relative to the camera axis, Ω. Thus, through Snell's Law, each of these angles has a set of accompanying refraction angles(δ, γ, α and β), unique to each value of Ω.

The positions of points A and B are related through the refraction angles, distance from the camera sensor and the tube dimensions to obtain the length of segment $\overline{BM}$ as represented in figure 7. The length of segment BM represents the distance between points A and B projected onto the plane of the camera sensor.

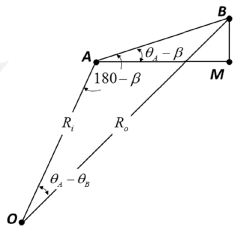

Figure 7: Geometric construct relating points A and B (0 represents the center of tube) with their projection onto the camera's aperture plane, figure from [5]

Then, considering both triangles formed in this geometrical construct and the sine law, one can extract the distance $\overline{AB}$ and then easily project it onto $\overline{BM}$, which will be the distance projected onto the camera plane sensor, as explained in equations 10 and 11.

$$AB = R_o \frac{sin(\theta_A - \theta_B)}{sin(180 - \beta)} \tag{10}$$

$$BM = ABsin(\theta_A - \theta_B) \tag{11}$$

The correction is applied to each point along the surface of the tube. First, the distance between points B and M must be calculated for each point along the meniscus surface, as described in equation 11. Then, each meniscus point is shifted horizontally by adding this quantity to its horizontal coordinate.

For example, considering a generic point along the meniscus of coordinates (x_i, y_i), where x_i is its horizontal coordinate and y_i is its vertical coordinate, the corrected position of this point will be given by (x_f, y_f), where $x_f = x_i + \overline{BM}$ and $y_f = y_i$.

This will result in a shift of all the points on the meniscus to the centre of the tube, as seen on figure 8 and predicted by [5].

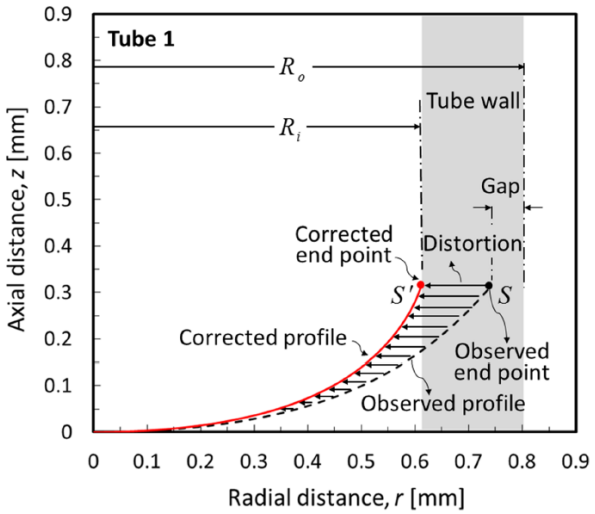

Figure 8: Effect of the correction on the meniscus, figure from [5]

The validation of the correction algorithm is displayed against the experimental data obtained in the U-tube setup in section 5.

4. Experimental test cases

4.1. Sessile droplet

The sessile droplet setup aimed to obtain the value of the static contact angle for the combination of HFE7200 and quartz substrate using the method described in references [31], [12] and [14]. The facility has four main components.

- A spark series SP-1200M-CXP4 high-speed industrial camera coupled to a Nikon-Mirror 105 mm 1:2.8 objective. The images captured by the camera were fed into the *GenICam* software, where the video file was assembled.
- A support for the quartz substrate where we deposited the droplet. This support was height adjustable and allowed better positioning within the picture frame.
- A diffused light source.
- A sterilized mono-use graduated syringe containing the liquid and mounted on optical support to ensure that the liquid droplets were placed in the imaging plane of the camera and were consistent with the calibration for the scaling of the images.

We analysed the pictures using image processing techniques implemented in a Python environment. The images were imported using *OpenCV* library and de-noised using a non-local mean filter. Then, the edges of the interface are detected using the approach described in [1], which consists in computing the image gradient through a convolution with Sobel-like kernel shown in 12 and identifying the peak gradient value using the *find peaks* function from the *Scipy* library.

$$Kernel = \begin{bmatrix} -E \\ C \\ E \end{bmatrix} \tag{12a}$$

$$E = \begin{bmatrix} 1 & 2 & 1 \\ 1 & 2 & 1 \\ 1 & 2 & 1 \end{bmatrix} \tag{12b}$$

$$C = \begin{bmatrix} 0 & -1 & 0 \\ 0 & 0 & 0 \\ 0 & 1 & 0 \end{bmatrix} \tag{12c}$$

Once the edges are detected, a fit is performed to the detected points of the droplet surface, with the surface's contact angle being the free parameter of the regression, as described in the previous section. We use the *curve fit* function from the *Scipy* library to minimise the non-linear least squares difference between the detected points and the solution of equation 2 to obtain the best contact angle for the experimental points.

4.2. 2D parallel plates

For the bi-dimensional quasi-capillary parallel plates, the set-up consisted of a channel section through which the liquid rises and a liquid reservoir. The channel section consists of two parallel quartz plates with a distance of $5\,$mm and closed at both ends. The liquid rises into the channel from a reservoir where the plates were submerged by about $6\,$mm. Then, we pressurised this reservoir to propel the fluid through the channel. The pressure was released to the reservoir via an electronically operated pressure valve. The pressure release time is recorded in a *Labview* routine, as well as the pressure values from pressure sensors located within the reservoir. The algorithm also records the camera start time, allowing to synchronise the images with the sensor data. The images are acquired with the same high-resolution camera described in the section 4.1 coupled with a Nikon-Mirror 105 mm 1:2.8 objective augmented with one magnification ring Nikon PK-13 27.5.

We observed the meniscus using the "Level Detection and Recording" technique [27]. This technique consisted in seeding HFE7200 with fluorescent particles of Pyrromethene 75820-500MG with a concentration of $6mg/L$. When hit by the green laser light, the particles emit fluorescent light toward the camera and show the shape of the meniscus in the plane of the laser. The laser sheet is produced by coupling a continuous green laser source with a concave and cylindrical lens. The concave lens was responsible for focusing the laser beam, and the cylindrical lens turned it into a laser sheet. The laser sheet impacts the liquid interface from a plane perpendicular to the 2D channel plates and the plane of the camera, as illustrated by figure 9.

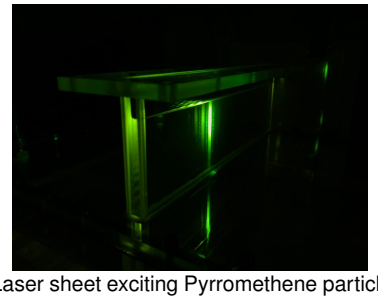

Figure 9: Laser sheet exciting Pyrromethene particles near the meniscus

These images were processed using the algorithm described in the previous section. This algorithm involves de-noising the images; applying a directional recontrasting filter which enhances the

intensity of the meniscus interface; detecting the edges using the gradient generated by the Sobel-like kernel [19] described in equation 12 and, finally, fitting equation 5 to the experimental points using the method described in sub-section 4.1.

We synchronised the interface shape and position data with the sensor data collected through the *Labview* routine, allowing us to label each image with the corresponding time stamp based on the starting time of the experiment, which corresponds to the pressure release.

For these experiments, four pressure points with reservoir over-pressures of 1510Pa, 1650Pa, 1850Pa and 1900Pa with three test runs each to ensure repeatability are considered.

4.3. U-tube setup

The U-tube is held vertically by a specially designed support. We uncovered the tube entrance to allow us to access the interior of the tube to place a grid with predetermined dimensions. The grid pattern enabled us to test the effects of optical distortion. A Python algorithm detected the vertical grid lines, and their position was corrected using the formulas for the optical correction shown in section 3.

The images are processed similarly to the previous two sections. However, the vertical lines were detected by searching for the local minima in the intensity of the image. The grid lines match the local minima for each horizontal line.

5. Results

5.1. Experiments with sessile droplets

The objective of the sessile droplet campaign was to obtain the static contact angle for HFE7200 over a quartz surface. These experiments are quite challenging due to the high volatility of HFE7200 and the extremely small contact angle to be observed. A droplet of HFE7200 quickly forms a thin film over the quartz plate and the droplet spreads unevenly over the surface. Figure 10 shows comparatively the large difference between a droplet of HFE7200 (on the right) and a droplet of water (on the left) on the same quartz surface. The latter forms a perfectly circular drop and shows a well defined point of contact with the solid surface. This is supported by the fact that sessile droplet technique are rarely used to observe contact angles below 15° [31] [12].

Figure 10: Captured image of a droplet of water and a droplet of HFE7200, where it is possible to see that the higher contact angle of water allows makes for a more clearly defined droplet

To capture images of a droplet of HFE7200 such as that seen in figure 10, the acquisition of the images needs to be fast, since the droplet evaporates very quickly, and requires to place the droplet consistently in the same place to avoid time lost focusing on the image and re-calibrating as described in sub-section 4.1.

The sessile droplet test yields a static contact angle of 6.23° for HFE7200 with a standard deviation of 3.53° over 20 different images. This uncertainty is higher than the generally accepted 2° encountered in sessile droplet tests.[31]

5.2. Static contact angle comparison with axial-symmetric meniscus

5.2.1 Characterization of optical distortion in cylindrical tube

To compare the results of the sessile droplet test campaign with contact angle measurements made in the quasi-capillary U-tube, it is necessary to correct the images of the latter for the optical distortion. To characterize the optical distortion, we considered equation 11 and measured the parameters L and Θ_0, the distance from the camera to the centre of the tube and the camera misalignment angle respectively. Both parameters are intrinsically difficult to measure by traditional means given the high uncertainty on the position of the center of the shutter. This process was improved by the introduction of an inverse method to estimate the above mentioned parameters.

The values of L and Θ_0 were obtained by comparing the corrected points to the positions of the grid lines printed in a transparent plastic film, which is inserted in the cylindrical tube in such a way that it adheres to the inner tube surface. Thus, the grid lines' positions are known and the values of L and Θ_0 optimized to retrieve the physical positions of the lines printed on the plastic film.

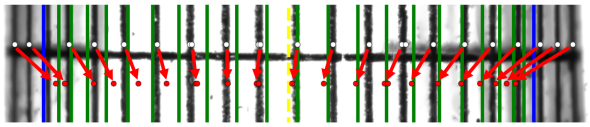

Figure 11: Distortion Results for Optimization of the L and Θ_0, where a section of the U-tube is displayed

Figure 11 represents a section of the U-Tube facility, where the algorithm has been applied. The white dots correspond to the algorithms' detection of the vertical grid lines which are distorted by curvature of the tube walls. The dashed yellow line marks the centre of the U-Tube and the two blue lines represent the inner tube walls. The green vertical lines correspond to the position of the vertical grid lines, if no distortion took place. The red dots represent the corrected position of each of the white dots. The arrows connecting each white dot with a red one help visualise the correction applied.

The points where the optical correction has been applied (in red) do not coincide with the green vertical lines, that represent the positions of the vertical grid lines if no optical distortion took place. This is due to the improper calculation of the position of the green lines. To generate them, the centre of the tube is considered to be unaffected by optical distortion and as a first approximation the camera misalignment is assumed to be null. In this case, the position of the true grid lines is obtained by considering the inner radius of the tube and the arc length between each of the vertical lines, which was imposed by the grid's design to be 0.2 mm long. Figure 12 shows the plot of the magnitude of the correction for several different camera misalignment angles and allows us to see the impact of this approximation.

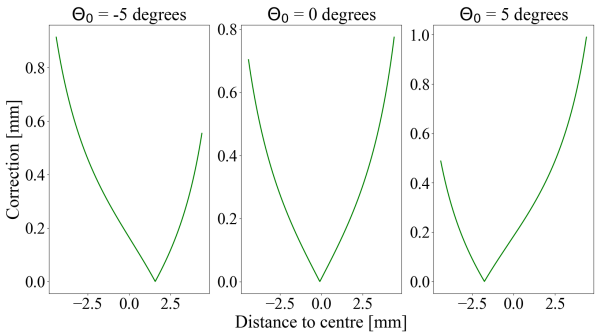

Figure 12: Influence of Θ_0 on the magnitude correction displayed for three different values of this variable

Figure 12 shows that for $\Theta_0 \neq 0$, the correction is not zero at the centre of the image. In this case the method becomes inaccurate and a new approach must be implemented in the inverse method. In this case the horizontal lines on the grid were considered. Since the grid wraps around the inner diameter, the length of each horizontal line corresponds to the inner diameter. Thus, by applying the correction to the outer points of the horizontal grid line (red), the corrected position coincide with the inner tube walls (vertical blue lines in figure 13). The true position of the inner walls is obtained using the calibration for the image scaling (see equation 13).

To perform this optimization only two points are available and given that the main difficulty in the experimental campaign was the measurement of the camera misalignment angle, only this parameter was optimised, keeping $L = 39cm$ as distance between the centre of the tube and the camera as measured during the experimental campaign. The optimization led to a $\Theta_0 = 0.77°$.

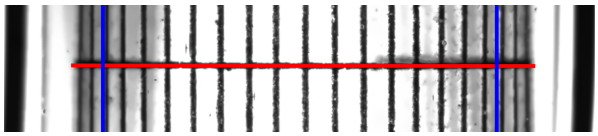

Figure 13: Figure with the detected horizontal line and the inner tube walls

$$\begin{cases} x_{firstWall} = (R_{outer} - R_{inner}) * pix2mm \\ x_{secondWall} = (R_{outer} + R_{inner}) * pix2mm \end{cases} \quad (13)$$

Figure 13 shows a new approach to evaluate the error associated with this method by comparing the length of the red line after the correction with the inner tube diameter given by the image calibration (distance between the blue lines). For the method applied here, this difference amounted to 4.64%. This error is slightly higher 3% which was the uncertainty obtained in [5]. This difference is attributed to lack of adherence of the grid to the tube walls and to the uncertainty on the distance to the tube, for future works the latter could be improved by using a laser distance measure.

5.2.2 Axial symmetric meniscus analysis

The optical correction of the previous section is applied to a set of quasi-capillary U-tube images as shown in figure 14.

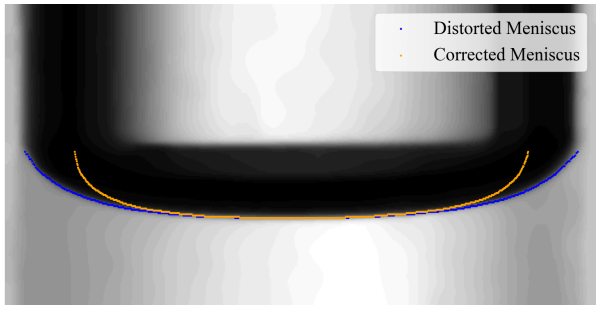

Figure 14: Figure with the detected meniscus interface in blue and the correction for the optical distortion of these points in orange

Figure 14 shows in blue the detected interface points and in orange the points corrected for the optical distortion. As expected, the interface points are shifted towards the center of the channel, in line with the predictions displayed in figure 13. The magnitude of the correction increases towards the edges of channel and it is very small at its center. As for the sessile droplet campaign, the contact angle is obtained through an optimisation procedure to match the experimental points with the solution to equation 2. The contact angles obtained went from $34.05\circ$ for the raw interface points to $8.55\circ$ for the case of the interface corrected for the optical distortion, emphasising the importance of correcting the data from this experimental set-up.

5.2.3 Static contact angle comparison across the three test-cases

The static contact angle in the 2D parallel plates setup is computed using the same approach described in the previous section, without the need to apply an optical correction due to the flat quartz walls in the front of the facility. We can now compare the static contact angle of both the sessile droplet and axial-symmetric meniscus configurations with the results obtained from the quasi-capillary parallel plates. In the latter, the contact angle measurement for images in static conditions led to an average static contact angle of $26.75 \circ \pm 4.67 \circ$. This is far different from the values obtained for the sessile droplet test and the quasi-capillary U-tube.

The contact angle should be independent of geometry, according to [15]. However, this is apparently not verified in the case of the 2D parallel plate facility. The difference between the axial-symmetric interfaces and the quasi-capillary parallel plates might be due to the detection of the interface. The resolution in the interface detection is very relevant for the measurement, given the degree of uncertainty associated with the wall positioning and the meniscus illumination near it which is also hard to account for. That might be responsible for this difference, since most likely the steepest part of the meniscus curvature is not visible in the images collected by means of "Level Detection and Recording" technique as can be seen in figure 15.

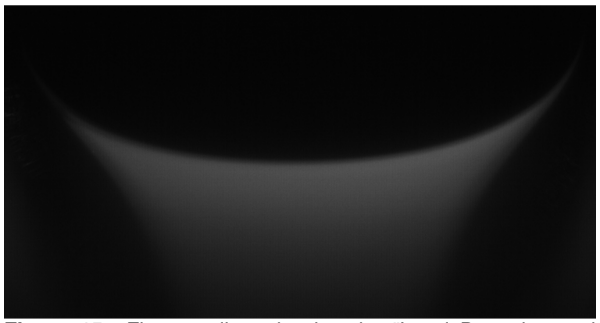

Figure 15: Figure collected using the "Level Detection and Recording" technique

5.3. Inertia-driven interface motion

In this section, the dynamic contribution to the contact angle is analysed by studying the motion of a 2D gas-liquid interface in a rectangular channel with width close to the capillary length of the test-fluid. The dynamic contact angle is measured with the technique described in sub-section 4.1 and compared with classic dynamic contact angle correlations.

The Hoffman-Tanner correlation [13] is the simplest correlation, which has also theoretical validation for the case of a steadily moving advancing contact line [28] and has been used as a basis to develop several other correlations [16]. The correlation establishes a linear relation between θ_D^3 and the capillary number, Ca.

$$\theta_d^3 - \theta_s^3 = a\text{Ca} \tag{14}$$

The capillary number corresponds to the non-dimensional contact line velocity and is defined as $\text{Ca} = \frac{\mu}{\sigma} V$. It relates the effect of the viscous forces with the effect of the surface tension forces. Constant a in 14 is within the interval [10-100] and needs to be found for the specific system under analysis. For this experimental campaign, this constant is calculated by minimising the difference between the experimental data and the proposed correlations. We achieved this by minimising a cost function that outputs the minimum square difference between the experimental data and the model solution.

Figure 16 plots the experimental dynamic contact angle (dots) and the prediction based on Hoffman's correlation (solid line) against the capillary number.

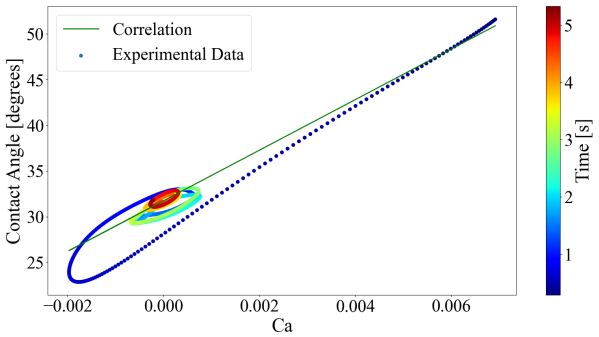

Figure 16: Experimental data for the contact angle plotted against time and the prediction by Hoffman-Tanner's correlation

In figure 16, the Hoffman-Tanner correlation predicts well the initial stages of the contact angle motion. After the initial descent, the experimental contact angle oscillates around the equilibrium position and shows multiple values for a given capillary number. Correlation 14 depends only on the capillary number and cannot account for these oscillations either over-estimating the dynamic contact angle in a receding contact line case or under-predicting the contact angle in the case of an advancing contact line.

Compared to the case considered in [13], the test-case analyzed here has several additional features. Two characteristics of the flow are considered as the reason for the mismatch: the cyclic behaviour of the history of the contact line and its acceleration. Reference [10] suggests the introduction of an unsteady term accounting for the rate of change of the dynamic contact angle and an additional term accounting for the dependency on the

acceleration of the contact line. This results in the following ordinary differential equation.

$$\alpha\dot{\Theta}' + \Theta' = a\mathsf{Ca} + b\mathsf{A} \tag{15}$$

In equation 15, A is the normalized contact line acceleration (i.e. it is divided by the gravitational acceeration) and $\Theta' = \theta_D^3 - \theta_S^3$. Equation 15 has also an analytical solution that is displayed in equation 16.

$$\Theta'(t) = \frac{1}{\alpha}e^{-\frac{t}{\alpha}}(a\int_0^t \mathsf{Ca}(t')e^{\frac{t'}{\alpha}}dt' + b\int_0^t \mathsf{A}(t')e^{\frac{t'}{\alpha}}dt') \tag{16}$$

Equation 16 shows that the full history of the capillary number and acceleration play a role in the determination of the dynamic contact angle. In addition to this, the solution also has a decay factor which would be responsible for an exponential decay of any disturbance in the meniscus shape, in agreement with the results of reference [23]. Figure 17 shows the comparison of the experimental contact angle with the prediction of equation 16 with the parameters optimized with the same procedure indicated above. The results of the optimization are indicated in table 1.

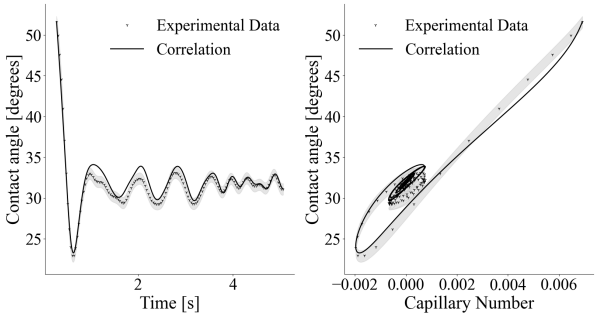

Figure 17: Figure displaying the results for the correlation proposed by Domenico Fiorini. On the left side the correlation predictions and experimental data for the contact angle are plotter against time and on the right side they are plotted against the capillary number

α	a	b
0.15	26.42	3.92

Table 1: Table with the optimised coefficients of equation 15

Figure 17 shows that the correlation is able to follow the orbits of the (unsteady) dynamic contact angle, with most oscillations falling within the uncertainty in the contact angle measurement.

The same coefficients of table 1 were tested against the data of the remaining pressure points with the same results.

Thus, equation 16 is considered an effective representation of the dynamic contact angle for this system. Now, the impact of the dynamic contact angle on the motion of the interface is evaluated as well as the possibility of obtaining the coefficients of the dynamic contact angle correlation not by fitting equation 16 to the experimental contact angle data but instead by solving equation 9, equipped with 15. The philosophy of this procedure falls aims to measure the dynamic contact angle without requiring the accurate visualization of the interface shape near to the contact line, which easily leads to possible high errors in the contact angle quantification as hypothesized in the static contact angle quantification.

To implement this method both equations 9 and 15 were coupled into a system of ordinary differential equations described in 17 and the contact angle correlation's coefficients are optimised using the experimental height data.

$$\begin{cases} \dot{h} = v \\ \dot{v} = f(h, v, \theta') \\ \dot{\theta}' = f(\theta', v, \dot{v}) \end{cases} \tag{17}$$

To achieve this, the model must predict accurately the motion. The system in equation 17 is solved using the initial conditions corresponding to the initial experimental point recorded, i.e. the first appearance of the meniscus within the field of view of the camera. The initial height is obtained from the experimental data and the interface velocity is considered as the average velocity given by ratio between the initial height and the corresponding time stamp. Figure 18 shows the comparison of the experimental interface height with the solution of equation 9. The model equation has both a higher frequency and a lower damping ratio than the experimental data.

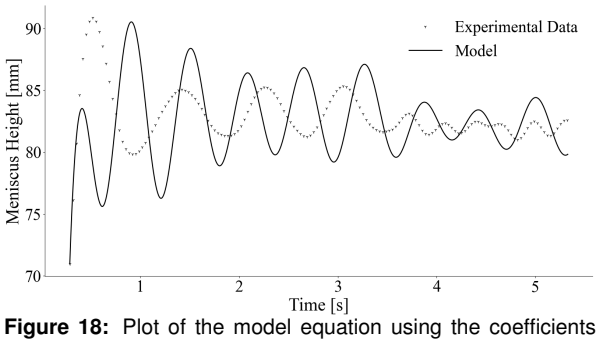

Figure 18: Plot of the model equation using the coefficients from the literature against the experimental data

Equation 9 has similarities to well-known second order systems such as the spring mass model where the natural frequency of the motion is given by equation 18. [11] [30]

$$\omega_n = \sqrt{\frac{k}{m}} \tag{18}$$

Thus, through the ratio of the frequencies of the experimental data and the model, a new added

mass term of $27.7 \times \frac{\delta}{2}$ [mm] is obtained, with the final value that resulted from the optimisation procedure being $50 \times \frac{\delta}{2}$ [mm]. Both terms represent a large increase in the coefficient that multiplies the characteristic width of the set-up, i.e. half the width of the channel. In reference [17], the characteristic width considered for the capillary tube is its radius and it is multiplied by $\frac{73}{60}$. However, in this reference creeping flow is considered and, thus, the range of Reynolds number considered is much smaller than the one obtained for the experimental data of Re $\simeq 200$, which would imply a significant difference in the phenomena description. Furthermore, the geometry described in [17] is a axial-symmetric which is not the case for the experimental set-up used. All in all, this results in the increase of the influence of the flow within the channel on the surrounding reservoir which leads to a higher added mass coefficient to make up for that difference.

Figure 18 also shows that the model predicts a lower damping ratio than the experiment data. Hence, the dissipative term is compiled in equation 19 and the impact of each of the three terms is evaluated.

$$\text{Dissipative Terms} = \left[\frac{12\mu}{\rho\delta^2}h + \frac{K_H\dot{h}}{2} + \frac{\mu K_C}{2\delta\rho}\right]\dot{h} \tag{19}$$

The average height is $\bar{h} = 50\,\text{mm}$, the channel thickness is $\delta = 5\,\text{mm}$ and an average vertical velocity of $\dot{h} = 2\text{mm/s}$. For the present fluid properties and coefficients given in the literature, $K_H = 7/3$ and $K_C = 4$, the Hagenbach-Couette correction represents about 20% of the total magnitude of the dissipative terms. However, if we consider the first oscillation of the liquid column where the vertical velocities are on average $\dot{h} = 200\text{mm/s}$, the Hagenbach-Couette correction assumes 95% of the total magnitude of the dissipative terms. So, we conducted an optimisation procedure for the Hagenbach-Couette coefficients based on the varying impact this correction has throughout the motion. This led us to $K_H = 1000$ and $K_C = 17.6$ which were used to generate the plot in figure 19.

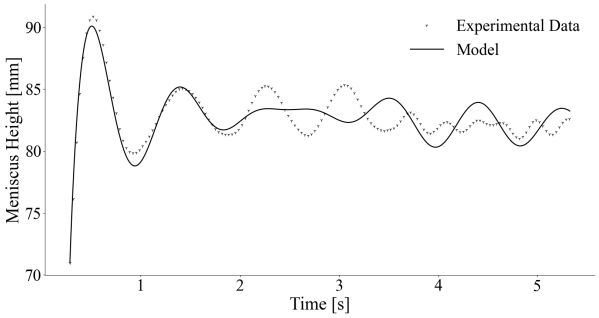

Figure 19: Plot of the optimised model equation predictions and the experimental data against time

Figure 19 shows the comparison of the experimental results with the model equation 9 including the optimised Hagenbach and Couette correction as well as the optimised added mass term. The coefficients obtained for the Hagenbach and Couette correction were quite different from the ones given in the literature for liquid rise in capillary tubes. In these experiments, the rise of the liquid is unidirectional, meaning that the height of the liquid column continually increases within the tube and no oscillations or downwards flow are observed. This presents a challenge for the prevailing models for capillary flow since the pressure loss term will have to be different for the times when liquid is going upward and downwards, since the flow characteristics at the entrance of the tube changes between those instances.

Moreover, in equation 19 the velocity profile has been simplified using the assumption of a steady Couette flow profile [24] . To better model this velocity profile and obtain a more representative viscous term, the model necessitates the inclusion of unsteady terms for the velocity profile. This is corroborated by the velocity profiles shown by PIV experiments done at the von Karman Institute for the same test-case [21].

Finally, the model's sensitivity to the surface tension term and the dynamic contact angle is analysed. Figure 20 shows the magnitude of the different forces of the model in equation 9, where each term has been computed using the experimental data.

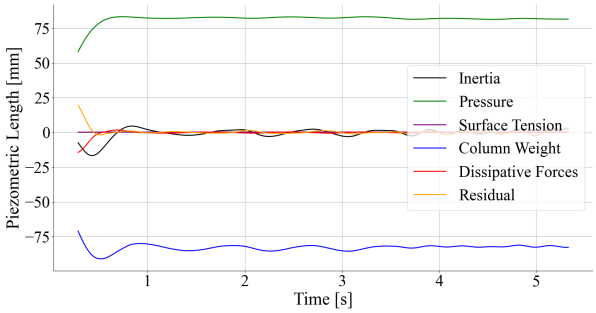

Figure 20: Plot of the forces produced by each term in the model equation as the height change they would produce in the liquid column

Each term in figure 20 is divided by $\rho \times g \times \delta$, making each term a geodetic pressure term. The main forces at play here are pressure and gravity, which both have identical modulus but different behaviours and would produce the same height change.

It is also interesting to note the role pressure plays on the dissipative term used in the model equation as can be observed in figure 21.

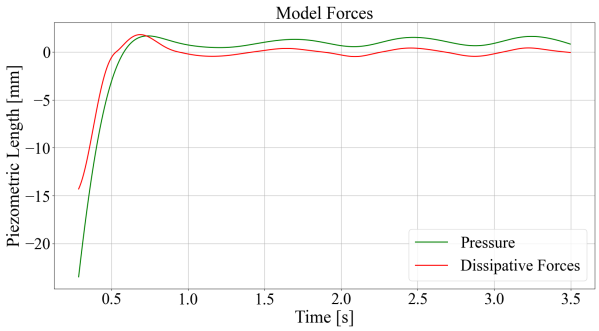

Figure 21: Plot of the pressure evolution in the reservoir against and dissipative term against time

The pressure term is also closely related with the dissipative term, with the velocity of the meniscus being mostly proportional to the pressure in the reservoir.

Figure 20 shows that the magnitude of the surface tension term is small compared to the other forces and the variation in contact angle would apparently produce a variation in the column height of only about 0.01 mm. To reinforce the idea that the contact angle plays very little role in this motion the model was solved for both the coefficients obtained by the previous optimization of the correlation for the dynamic contact angle and coefficients that were an order of magnitude higher. These results were plotted against the experimental data in figure 22.

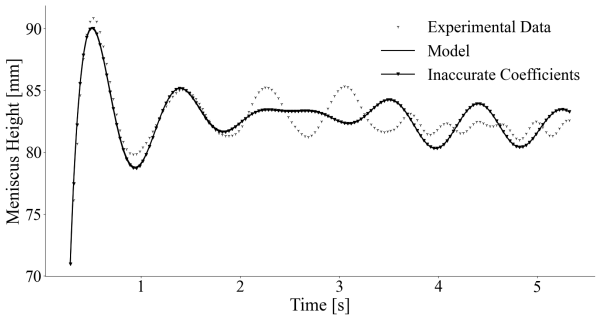

Figure 22: Plot of the experimental data against model predictions using the dynamic contact angle correlation coefficients obtained in the optimisation process and a random set of coefficients for this correlation

In figure 22 is possible to see that both solutions overlap almost perfectly, meaning that the model is not yet sensitive to major changes in the contact angle. It is also worth noting that the model is still not able to capture some of the frequencies in the later stages of the motion where three dimensional effects such as vibration modes in the longitudinal direction of the channel might be considerable.

6. Conclusion

In this experimental work, a detailed analysis of the contact angle formed by a gas-liquid interface with a solid surface was conducted. The contact angle in *static* conditions is a property of the fluid/substrate and should be independent of the specific geometry in use [15], while the *dynamic* contact angle depends on the kinematics of the flow.

For the static characterization three different test-case were compared: sessile droplet, circular tube, 2D parallel plates channel. The second geometry required correction for the optical distortions. The optical distortions were corrected using the algorithm proposed by [5], which involves measuring accurately the angle of misalignment of the camera Θ_0. An inverse method was employed to obtain the value for the parameter and improve accuracy. Using this method, the images of a meniscus were corrected in a cylindrical channel and compared against the sessile droplet test campaign and quasi-capillary 2D parallel plates. The *static* contact angle obtained from the latter facility was largely different from the two other cases, this is attributed to the poor meniscus illumination near the wall obtained by the ”Level Detection and Recording” technique.

The tests were extended to the 2D parallel plate setup to for dynamic conditions, characterizing the dynamic contact angle of a moving interface using a physical quasi-static model to fit of the interface shape. The results were compared with empirical contact angle correlations accounting for the acceleration of the contact line and its history and their impact on a integral model for the rise of the interface in the 2D channel was tested. This aimed to replace the need for an accurate observation of the interface to measure the contact angle.

The empirical correlations accounted for the acceleration of the contact line and in doing so it described well the dynamic contact angle, while this is not the case for traditional correlations accounting only for the contact line velocity. On the other hand, the integral model for the interface rise based on the prevailing models for capillary flow within the quasi-capillary parallel plates struggled to describe the phenomena accurately. This implied the model not being sensitive enough to the surface tension term to allow the implementation of a method that optimises the coefficients for the dynamic contact angle correlation using only the history of the interface motion.

Thus, future work should focus on improving the model to make this possible. This could possibly be done by including terms, which account for the unsteady behaviour of the motion of the interface and a model that accounts for the varying conditions in the tube entrance. In addition to this, better detection near the walls using the LEDar method is required to verify the dependence of the *static* contact angle on the solid/fluid combination alone.

References

[1] A. Alazzawi, H. Alsaadi, A. Shallal, and S. Albawi. Edge detection-application of (first and second) order derivative in image processing. 12 2015.

[2] A. Alghunaim, S. Kirdponpattara, and B. min Zhang Newby. Techniques for determining contact angle and wettability of powders. *Powder Technology*, 287:14, 2016.

[3] B. Arouxet, N. Echebest, and E. Pilotta. Active-set strategy in powell's method for optimization without derivatives. *Computational Applied Mathematics*, 30:25, 07 2016.

[4] D. C. Bogue. Entrance effects and prediction of turbulence in non-newtonian flow. *Industrial & Engineering Chemistry*, 51(7):4, 1959.

[5] M. Darzi and C. Park. Optical distortion correction of a liquid-gas interface and contact angle in cylindrical tubes. *Physics of Fluids*, 29(5), 2017.

[6] M. Deserno. The shape of a straight fluid meniscus, 2005. Lecture notes Max-Planck Institute For Polymer Research, Mainz, Germany.

[7] S. Deutsch. A preliminary study of the fluid mechanics of liquid penetrant testing. *Journal of research of the National Bureau of Standards*, 84:6, 1979.

[8] N. V. K. Dutt. Determination of hagenbach and coutte correction factors for the flow of power law fluids. *Physics and Chemistry of Liquids*, 35(4):17, 1998.

[9] A. Eales, N. Dartnell, S. Goddard, and A. Routh. Evaporation of pinned droplets containing polymer - an examination of the important groups controlling final shape. *AIChE Journal*, 61, 02 2015.

[10] D. Fiorini. Dynamic contact angle analysis using inverse methods. 12th Symposium of VKI PhD Research. von Karman Institute, 2021. Under Revision.

[11] G. Franklin, J. Powell, and A. Emami-Naeini. *Feedback Control Of Dynamic Systems*. 01 1994.

[12] S. R. Friedman, M. Khalil, and P. Taborek. Wetting transition in water. *Phys. Rev. Lett.*, 111:5, Nov 2013.

[13] R. L. Hoffman. A study of the advancing interface. i. interface shape in liquid—gas systems. *Journal of Colloid and Interface Science*, 50(2):13, 1975.

[14] K. J. Huhtamäki T., Tian X. Surface-wetting characterization using contact-angle measurements. *Nature Protocols*, 13:17, 2018.

[15] T.-S. Jiang, O. Soo-Gun, and J. C. Slattery. Correlation for dynamic contact angle. *Journal of Colloid and Interface Science*, 69(1):4, 1979.

[16] S. F. Kistler. The hydrodynamics of wetting. *Wettability*, 1993.

[17] S. Levine, J. Lowndes, E. J. Watson, and G. Neale. A theory of capillary rise of a liquid in a vertical cylindrical tube and in a parallel-plate channel: Washburn equation modified to account for the meniscus with slippage at the contact line. *Journal of Colloid and Interface Science*, 73(1):15, 1980.

[18] M. Lowe and P. Kutt. Refraction through cylindrical tubes. *Experiments in Fluids*, 13(5):315–320, 1992.

[19] M. A. Mendez, L. Németh, and J. M. Buchlin. Measurement of Liquid Film Thickness via Light Absorption and Laser Tomography. In *European Physical Journal Web of Conferences*, volume 114 of *European Physical Journal Web of Conferences*, 2016.

[20] F. D. R. Philipp Behruzi and F. Cirillo. *Coupling sloshing, GNC and rigid body motions during ballistic flight phases*.

[21] M. Ratz. Experimental analysis of contact line dynamics using optical techniques and inverse methods. Master's thesis, Technische Fakultät Praktikumsarbeit Universität, 2021.

[22] A. Rudawska and E. Jacniacka. Analysis for determining surface free energy uncertainty by the owen–wendt method. *International Journal of Adhesion Adhesives*, (29):6, 2009.

[23] J. Snoeijer, B. Andreotti, G. Delon, and M. Fermigier. Relaxation of a dewetting contact line part 1: A full-scale hydrodynamic calculation. *Journal of Fluid Mechanics*, 579, 06 2007.

[24] E. M. Sparrow, S. H. Lin, and T. S. Lundgren. Flow development in the hydrodynamic entrance region of tubes and ducts. *The Physics of Fluids*, 7(3):338–347, 1964.

[25] M. Stange, M. Dreyer, and H. Rath. Capillary driven flow in circular cylindrical tubes. *Physics of Fluids*, 15, 08 2003.

[26] J. Szekely, A. Neumann, and Y. Chuang. The rate of capillary penetration and the applicability of the washburn equation. *Journal of Colloid and Interface Science*, 35(2):5, 1971.

[27] B. Toth, J. Anthoine, and J. Steelant. Cryogenic sloshing investigation by means of non-intrusive measurement techniques. page 14, 2016.

[28] O. V. Voinov. Hydrodynamics of wetting. *Fluid Dynamics*, (11):7, 1976.

[29] E. W. Washburn. The dynamics of capillary flow. *Phys. Rev.*, 17:10, Mar 1921.

[30] B. Yang. Theory of vibration — fundamentals. In S. Braun, editor, *Encyclopedia of Vibration*, pages 1290–1299. Elsevier, Oxford, 2001.

[31] Y. Yuan and T. R. Lee. Contact angle and wetting properties. In *Surface Science Techniques*, Springer Series in Surface Sciences. Springer Berlin, Heidelberg, 2013.